Polarisation of the Balmer-α emission in crossed electric and magnetic fields

Alex Thorman

PII: S0022-4073(17)30669-6
DOI: 10.1016/j.jqsrt.2017.12.015
Reference: JQSRT 5931

To appear in: *Journal of Quantitative Spectroscopy & Radiative Transfer*

Received date: 30 August 2017
Revised date: 19 October 2017
Accepted date: 18 December 2017

Please cite this article as: Alex Thorman, Polarisation of the Balmer-α emission in crossed electric and magnetic fields, *Journal of Quantitative Spectroscopy & Radiative Transfer* (2017), doi: 10.1016/j.jqsrt.2017.12.015

Highlights

- A corrected model of the Balmer-α polarisation in crossed fields is presented.
- The σ_o polarisation orientation is always orthogonal to the electric field.
- The $\sigma_{\pm1}$ polarisation orientation may deviate under certain conditions.
- The $\sigma_{\pm1} : \pi_{\pm3}$ intensity ratio may also deviate

Polarisation of the Balmer-α emission in crossed electric and magnetic fields

Alex Thorman

Plasma Research Laboratory, Research School of Physics and Engineering, Australian National University, Canberra, ACT 0200, Australia

Abstract

An analysis of the polarisation structure of the Balmer-α emission in the presence of electric and magnetic fields is presented, with an emphasis on motional Stark effect polarimetry for fusion plasma diagnostics. When the fields are orthogonal, as is the case for neutral heating beams injected into a magnetised plasma, some degeneracy remains in the Stark-Zeeman energy levels and the magnetic quantum number is not well defined. The polarisation structure from the degenerate states is underdetermined and therefore volatile to weaker interactions that resolve this degeneracy, a critical subtlety that has previously been overlooked. A perturbation theory analysis finds distinct polarisation structures for the σ emission that apply when the fine-structure and microscopic electric fields are considered. It is found that only the $\sigma_{\pm 1}$ polarisation orientation is sensitive to upper-state populations (which are non-statistically weighted for neutral beam injection into a target gas), but with appropriate viewing geometries and beam injection directions the effect can be made negligible.

1. Introduction

Measurement of the Balmer-alpha polarisation orientation in the presence of a motional electric field is the most widely used diagnostic technique for constraining the magnetic field inside a magnetic confinement fusion device. So called Motional Stark effect (MSE) polarimeters observe the Doppler shifted emission from a high energy neutral deuterium (or hydrogen) beam injected into the plasma[1, 2]. The beam atoms with velocity $\mathbf{v}$ in a magnetic field $\mathbf{B}$ experience a motional electric field, $\mathbf{E_L} = \mathbf{v} \times \mathbf{B}$, in their rest

frame. The Stark effect splits the emission into discrete π and σ lines that are polarised parallel and perpendicular to the electric field respectively[3].

MSE polarimetry is considered to be a mature diagnostic technique, nevertheless existing models of the polarisation spectrum are flawed. This is particularly evident when the upper-states of the transition are non-statistically populated. For example a proposed MSE line ratio measurement technique[4] asserts that σ_1 and π_3 emissions derive from the same upper-states, contrary to atomic modelling that found the σ_1 emission can derive from an upper-state free of any π_3 emission[5]. As another example, a collisional radiative model that predicts the σ_0 polarisation orientation is dependent on upper-state populations contains a critical bug[6, 7]. An independent model that also predicts this σ_0 effect ignores the remaining degeneracy in the system[8, 9].

The sensitivity of the polarisation to upper-state populations is pertinent because plasma densities in modern fusion devices are not sufficiently large for the upper-states to achieve equal populations obeying Boltzmann statistics[2, 10]. Beam into gas (BIG) is a desirable in-vessel calibration technique for MSE polarimeters that observes the neutral beam injected into gas with a known magnetic field. However the gas densities are lower than the standard plasma densities resulting in an enhanced upper-state population disparity. The validity of BIG calibration is contentious and the technique has been abandoned on some devices owing the upper-state population dependent σ_0 polarisation orientation findings[8, 6] and the effect of secondary neutrals[11].

The discrepancies in existing polarimetric models stem from the implementation of the Zeeman effect and weaker interactions. At first this is surprising given that the Stark splitting is typically more than five times greater than these other splitting mechanisms. These discrepancies only become clear after the underdetermined nature of the degenerate Stark-Zeeman states and the subtle differences between various orthogonalisations of these states is understood. This is elucidated in sections 3 and 4 where two distinct Stark-Zeeman solutions are presented. It is not possible to determine the system when only the Stark and Zeeman effects are considered, hence further weaker interactions are essential to resolving the ambiguity. The fine-structure of the atom and microscopic fields within the plasma are the largest of these interactions and their influence is considered in sections 5 and 6 respectively.

2. Background

Dimensional parameters, ϵ and γ, commonly used for the Stark and Zeeman energy splitting respectively are

$$\epsilon = 3ea_0|\mathbf{E}|, \tag{1}$$

$$\gamma = \frac{e\hbar}{2m_e}|\mathbf{B}|, \tag{2}$$

$$q_0 = \sqrt{\epsilon^2 + \gamma^2}, \tag{3}$$

$$q_1 = \sqrt{9\epsilon^2 + 4\gamma^2}, \tag{4}$$

where e is the elementary charge, a_0 is the Bohr radius, $\hbar$ is the reduced Planck constant and m_e is the mass of the electron. $\gamma/\epsilon \sim 0.1$ for typical fusion neutral beam injection energies ($\sim$ 100keV). Often this ratio is underestimated creating the impression that the Zeeman effect can always be neglected, however more recent studies have identified circumstances where it cannot be disregarded[12, 13].

The parabolic states $|n, k, m\rangle$ are the natural solution for the pure Stark effect, where n is the principle quantum number, m is the magnetic quantum number and $k = n_1 - n_2$, with parabolic quantum numbers $n_1 \geq 0$ and $n_2 \geq 0$ such that $n_1 + n_2 + 1 = n - |m|$. Parabolic states with the same values of n and k are degenerate. The states are necessarily eigenstates of the projected angular momentum operator L_z with eigenvalue $m\hbar$. Transitions with $\Delta m = 0$, known as π, are polarised parallel to the electric field while transitions with $\Delta m = \pm 1$, known as $\sigma^{\pm}$, have linear polarisation perpendicular to the electric field.

The calculation procedure used here (described in Appendix A) is similar to that detailed in Ref. [14], however for comparison with the parabolic states of the pure Stark effect our coordinate system is oriented with the electric field along the z-axis, as described in Fig. 1. The polarimeter axes are oriented such that the external electric field and π polarisation is at 90°.

3. Stark-Zeeman effect

When the magnetic field is orthogonal to the electric field the degree of degeneracy is the same as pure Stark effect case. This well-known result[9]

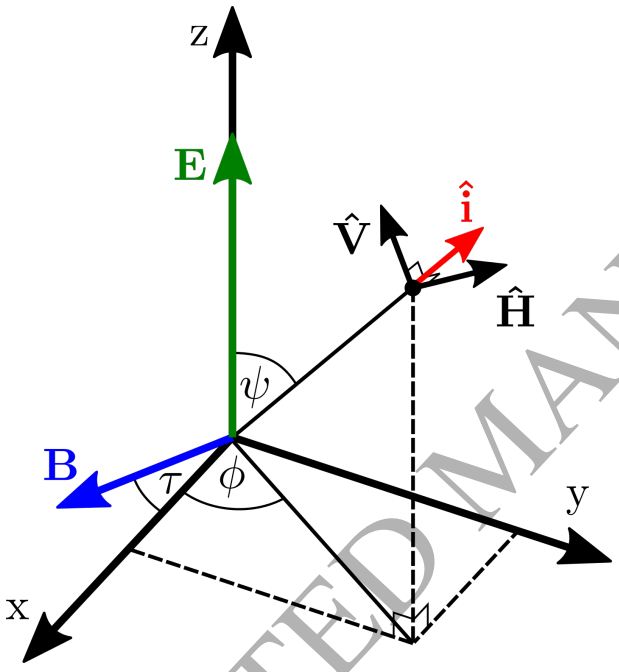

Figure 1: Coordinate system used throughout the paper. The electric field lies in the z-axis. For a pure motional electric field the magnetic field lies in the x-axis, but here for generality, it is allowed an inclination angle τ in the xz-plane. The emission is viewed from direction $\mathbf{i}$ with polar angle ψ and azimuthal angle ϕ. Without loss of generality the horizontal axis of the polarimeter is orthogonal to the electric field such that $\mathbf{H} = \mathbf{E} \times \hat{\mathbf{i}}$. The vertical axis of the detector is then $\hat{\mathbf{V}} = \hat{\mathbf{i}} \times \hat{\mathbf{H}}$.

is displayed in Fig. 2. However, there is a crucial difference between Stark-Zeeman and pure Stark effect. A superposition of degenerate parabolic states is a valid solution of the perturbed Hamiltonian, but the requirement for rotational invariance about the electric field prevents such a superposition. That is, for the pure Stark effect the magnetic quantum number m distinguishes the degenerate states. However the $\mathbf{L}\cdot\mathbf{r}$ operator cannot commute with both the Stark and Zeeman Hamiltonians, implying the magnetic quantum number m is not valid for the Stark-Zeeman effect. Furthermore the requirement for rotational invariance is lost with crossed fields such that any superposition/orthogonalisation of degenerate states is a valid solution. Essentially the magnetic field decreases the symmetry within the system without decreasing the degeneracy, hence the degenerate Stark-Zeeman states are underdetermined.

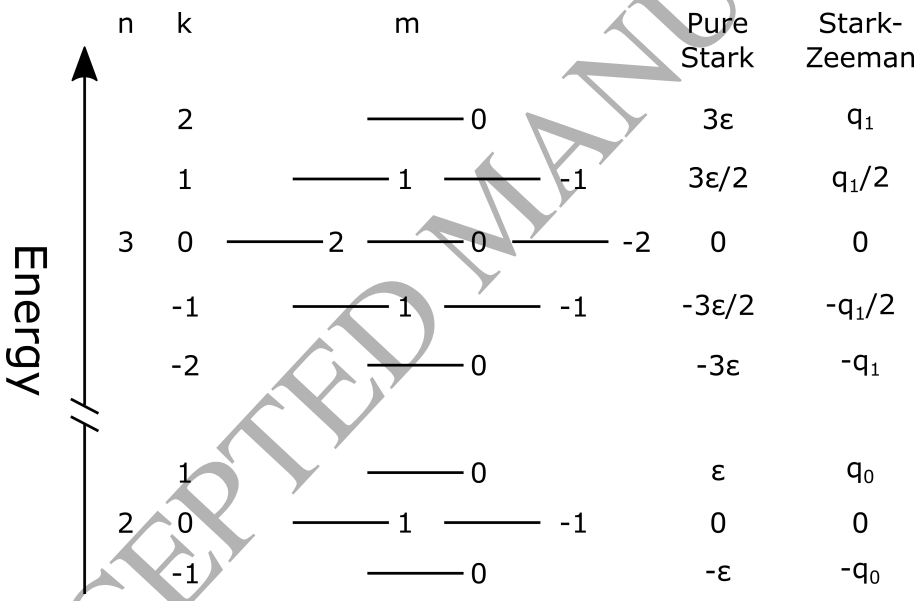

Figure 2: Energy and degeneracy of the n=2 and n=3 levels of the pure Stark states and Stark-Zeeman states. In the Stark-Zeeman case the degeneracy only exists when the electric and magnetic fields are orthogonal.

The first new Stark-Zeeman orthogonalisation we consider is that which converges with the parabolic states as $\gamma/\epsilon \to 0$. When $\mathbf{B}$ is non-orthogonal to $\mathbf{E}$ ($\tau \neq 0$ in Fig. 1) the energy levels are all non-degenerate and therefore the states are all well-defined/determined. In this more general case the energy

levels are given by:

$$E_{|2,\pm1,0\rangle} = \pm \frac{1}{\sqrt{2}}\sqrt{q_0^2 + \sqrt{q_0^4 - 4\gamma^2\epsilon^2\sin^2\tau}}, \tag{5}$$

$$E_{|2,0,\pm1\rangle} = \pm \frac{1}{\sqrt{2}}\sqrt{q_0^2 - \sqrt{q_0^4 - 4\gamma^2\epsilon^2\sin^2\tau}}, \tag{6}$$

$$E_{|3,\pm2,0\rangle} = \pm \frac{1}{\sqrt{2}}\sqrt{q_1^2 + \sqrt{q_1^4 - 144\gamma^2\epsilon^2\sin^2\tau}}, \tag{7}$$

$$E_{|3,0,0\rangle} = 0 \tag{8}$$

$$E_{|3,0,\pm2\rangle} = \pm \frac{1}{\sqrt{2}}\sqrt{q_1^2 - \sqrt{q_1^4 - 144\gamma^2\epsilon^2\sin^2\tau}}, \tag{9}$$

$$E_{|3,1,\pm1\rangle} = \frac{1}{2}\sqrt{q_1^2 \pm 12\gamma\epsilon\sin\tau}, \tag{10}$$

$$E_{|3,-1,\pm1\rangle} = -\frac{1}{2}\sqrt{q_1^2 \mp 12\gamma\epsilon\sin\tau}. \tag{11}$$

Evidently when $\tau = 0$ the partially degenerate Stark-Zeeman energy levels in Fig. 2 are returned. Taking the limit $\tau \to 0$ for these generalised states delivers the parabolic like Stark-Zeeman states, which we label $|n, k, m\rangle_C$ (where 'C' denotes 'circular'). This particular set of states is the only Stark-Zeeman solution that converges to the parabolic states when $\gamma \ll \epsilon$ and the quantum number m therefore maintains some relevance. Mixing coefficients for these new Stark-Zeeman states are presented in the Appendix in Tables B.3 for n=2 and B.4 for n=3.

A quantitative summary of the intensity, type and energy for the $n = 3 \to 2$ transitions is presented in Table 1. With the coordinate system defined in Fig. 1 the dimensionless Stokes vector (described in Appendix A) for each transition, when $\gamma \ll \epsilon$, is:

$$\bar{\mathbf{s}}_\pi = (\sin^2\psi,\, -\sin^2\psi,\, 0,\, 0), \tag{12}$$

$$\bar{\mathbf{s}}_{\sigma^\pm} = \frac{1}{2}(1 + \cos^2\psi,\, \sin^2\psi,\, 0,\, \pm 2\cos\psi). \tag{13}$$

The π emission is a projection of a dipole oscillation along the electric field axis. The $\sigma^\pm$ emissions are produced from circular dipole orbits in the plane perpendicular to the electric field which project as ellipses along the line of sight, illustrated in Fig. 3a). The $\sigma^\pm$ linear polarisation orientations, given

$\|n,k,m\rangle_C$	$\|2,1,0\rangle_C$	$\|2,-1,0\rangle_C$	$\|2,0,1\rangle_C$	$\|2,0,-1\rangle_C$
$\|3,2,0\rangle_C$	$(1681)\pi_4$	$(1)\pi_8$	$(18)\sigma_6^+$	$(18)\sigma_6^-$
$\|3,-2,0\rangle_C$	$(1)\pi_{-8}$	$(1681)\pi_{-4}$	$(18)\sigma_{-6}^+$	$(18)\sigma_{-6}^-$
$\|3,0,0\rangle_C$	$(729)\pi_{-2}$	$(729)\pi_2$	$(882)\sigma_0^+$	$(882)\sigma_0^-$
$\|3,0,2\rangle_C$	-	-	$(4608)\sigma_0^-$	-
$\|3,0,-2\rangle_C$	-	-	-	$(4608)\sigma_0^+$
$\|3,1,1\rangle_C$	$(1936)\sigma_1^-$	$(16)\sigma_5^-$	$(1152)\pi_3$	-
$\|3,1,-1\rangle_C$	$(1936)\sigma_1^+$	$(16)\sigma_5^+$	-	$(1152)\pi_3$
$\|3,-1,1\rangle_C$	$(16)\sigma_{-5}^-$	$(1936)\sigma_{-1}^-$	$(1152)\pi_{-3}$	-
$\|3,-1,-1\rangle_C$	$(16)\sigma_{-5}^+$	$(1936)\sigma_{-1}^+$	-	$(1152)\pi_{-3}$

Table 1: Transitions between n=3 and n=2 states for the Stark-Zeeman $|n,k,m\rangle_C$ states in the limit $\gamma/\epsilon \to 0$. The format is $(Intensity)Type_{\text{Energy}}$ where the distinction between handedness of the σ transition is made with + and - superscripts. The magnitude of the dipole vector is related to the intensity in the parenthesis via the relationship $|r_{ij}|^2 = 2^{14}3^6a_0^2(Intensity)/5^{14}$. As expected the transition probabilities are the same as Table 20b of Ref. [3] for the pure Stark effect.

by the major axis of the ellipses, are both orthogonal to the π polarisation when $\gamma \ll \epsilon$ regardless of the viewing angle. This orthogonality of σ^+ and σ^- to π is also evident from Eqs. 12 and 13. Hence the σ orientation is independent of the $\sigma^+ : \sigma^-$ intensity ratio and the polarisation structure is therefore referred to as a 'robust'.

Evidently we have found the Stark-Zeeman solutions that predict similar results to the pure Stark theory when $\gamma \ll \epsilon$. However the degenerate Stark-Zeeman states are underdetermined and other possible superpositions must also be considered.

4. Physically relevant alternative Stark-Zeeman states

Here a second distinct Stark-Zeeman solution is presented where the degenerate states are orthogonalised differently to the 'circular states' of the previous section. These new states are labelled $|n,k,\tilde{m}\rangle_L$ (where 'L' denotes 'linear') and their physical relevance will become clear in Sec. 5 when the fine structure of the atom is considered.

$|3,0,0\rangle_C$ and the non-degenerate states are the same for the 'C' and 'L' Stark-Zeeman solutions. The remaining $|n,k,\tilde{m}\rangle_L$ states are formed using

the relationships:

$$\left|2,0,\pm\tilde{1}\right\rangle_L = \frac{1}{\sqrt{2}}\left(|2,0,1\rangle_C \mp |2,0,-1\rangle_C\right), \tag{14}$$

$$\left|3,0,\pm\tilde{2}\right\rangle_L = \frac{1}{\sqrt{2}}\left(|3,0,2\rangle_C \pm |3,0,-2\rangle_C\right), \tag{15}$$

$$\left|3,1,\pm\tilde{1}\right\rangle_L = \frac{1}{\sqrt{2}}\left(|3,1,1\rangle_C \mp |3,1,-1\rangle_C\right), \tag{16}$$

$$\left|3,-1,\pm\tilde{1}\right\rangle_L = \frac{1}{\sqrt{2}}\left(|3,-1,1\rangle_C \mp |3,-1,-1\rangle_C\right). \tag{17}$$

These new states are valid solutions to the perturbed Hamiltonian but do not converge with the parabolic states when $\gamma \to 0$. The observable differences between the $|n,k,m\rangle_C$ and $|n,k,\tilde{m}\rangle_L$ solutions are now described and for simplicity the limit that $\gamma \ll \epsilon$ is considered.

For the $|n,k,m\rangle_C$ states we have that $\langle L_z\rangle_C = m\hbar$ whereas for the $|n,k,\tilde{m}\rangle_L$ states we have that $\langle L_z\rangle_L = 0$. Hence the tilde notation is used as the quantum number m is never valid for these $|n,k,\tilde{m}\rangle_L$ states in Eqs. 14-17, but the value is kept for identification purposes. The σ polarisation structure for the $|n,k,\tilde{m}\rangle_L$ basis is significantly different to the $|n,k,m\rangle_C$ basis, stemming from the result that $\Delta\langle L_z\rangle_L = 0$ as opposed to $\Delta m \equiv \Delta\langle L_z\rangle_C/\hbar = \pm 1$. Consequently the σ dipole vectors from the $|n,k,\tilde{m}\rangle_L$ states now oscillate linearly along the $\mathbf{B}$ and $\mathbf{E}\times\mathbf{B}$ direction and are referred to as σ^B and σ^v emissions respectively (using the notation of Ref. [8]). This alternate polarisation structure is illustrated in Fig. 3b).

A quantitative summary of the intensity, type and energy of each transition are listed in Table. 2. The dimensionless Stokes vectors for the σ^v and σ^B transitions are:

$$\begin{aligned}\bar{\mathbf{s}}_{\sigma^B} =&(\sin^2\phi + \cos^2\psi\cos^2\phi,\\ &\sin^2\phi - \cos^2\psi\cos^2\phi,\ \cos\psi\sin 2\phi,\ 0),\end{aligned} \tag{18}$$

$$\begin{aligned}\bar{\mathbf{s}}_{\sigma^v} =&(\cos^2\phi + \cos^2\psi\sin^2\phi,\\ &\cos^2\phi - \cos^2\psi\sin^2\phi,\ -\cos\psi\sin 2\phi,\ 0).\end{aligned} \tag{19}$$

The σ^B and σ^v linear polarisation orientations are dependent on the viewing direction and are generally different. Hence their combined net linear polarisation orientation is dependent on their relative transition rates and relative upper-state populations. Only when σ^B and σ^v have the same emission rate

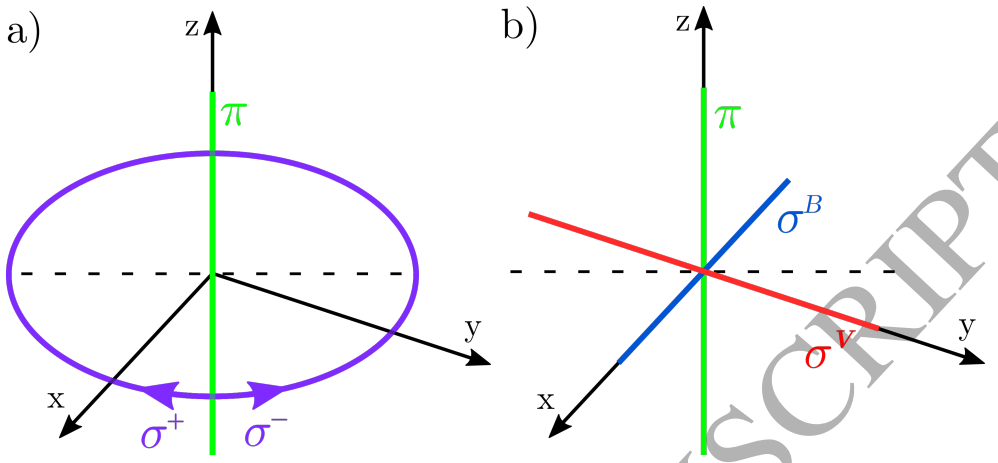

Figure 3: a) Polarisation structure of the $|n,k,m\rangle_C$ transitions in the limit $\gamma/\epsilon \to 0$. The major axis of the $\sigma^{\pm}$ ellipses, depicted with the dashed line, are always perpendicular to the electric field projection. b) Polarisation structure of the $|n,k,\tilde{m}\rangle_L$ transitions in the limit $\gamma/\epsilon \to 0$. An equal emission rate of σ^B and σ^v transitions combine to produce a partial linear polarisation orthogonal to the π emission, depicted by the dashed line.

is the net linear polarisation perpendicular to π as,

$$\bar{\mathbf{s}}_{\sigma^B} + \bar{\mathbf{s}}_{\sigma^v} = \bar{\mathbf{s}}_{\sigma^+} + \bar{\mathbf{s}}_{\sigma^-}. \tag{20}$$

An unequal rate of $\sigma^{\pm}$ emissions produces a net s_3 component without affecting the linear polarisation orientation. Whereas here an unequal rate of σ^B and σ^v emissions produces a net s_2 component, implying that σ is not guaranteed to be perpendicular to π or a true measure of the orientation of $\mathbf{E}$. Importantly there is no contaminating s_2 component when viewing with $\psi = \pi/2$ or $\phi = n\pi$ which are generally targeted for MSE measurements to achieve the greatest polarisation fraction and maximise the radial resolution respectively.

The net linear polarisation orientation of a particular σ line can be calculated using Eqs. 18 and 19. If the σ^B emission has transition rate A_B deriving from an upper-state with population N_B and the σ^v emission has transition rate A_v deriving from an upper-state with population N_v then the

$\lvert n,k,\tilde{m}\rangle_L$	$\lvert 2,1,0\rangle_L$	$\lvert 2,-1,0\rangle_L$	$\lvert 2,0,\tilde{1}\rangle_L$	$\lvert 2,0,-\tilde{1}\rangle_L$
$\lvert 3,2,0\rangle_L$	$(1681)\pi_4$	$(1)\pi_8$	$(18)\sigma_6^B$	$(18)\sigma_6^v$
$\lvert 3,-2,0\rangle_L$	$(1)\pi_{-8}$	$(1681)\pi_{-4}$	$(18)\sigma_{-6}^B$	$(18)\sigma_{-6}^v$
$\lvert 3,0,0\rangle_L$	$(729)\pi_{-2}$	$(729)\pi_2$	$(882)\sigma_0^B$	$(882)\sigma_0^v$
$\lvert 3,0,\tilde{2}\rangle_L$	-	-	$(2304)\sigma_0^v$	$(2304)\sigma_0^B$
$\lvert 3,0,-\tilde{2}\rangle_L$	-	-	$(2304)\sigma_0^B$	$(2304)\sigma_0^v$
$\lvert 3,1,\tilde{1}\rangle_L$	$(\mathbf{1936})\sigma_{\mathbf{1}}^{\mathbf{B}}$	$(16)\sigma_5^B$	$(1152)\pi_3$	-
$\lvert 3,1,-\tilde{1}\rangle_L$	$(\mathbf{1936})\sigma_{\mathbf{1}}^{\mathbf{v}}$	$(16)\sigma_5^v$	-	$(1152)\pi_3$
$\lvert 3,-1,\tilde{1}\rangle_L$	$(16)\sigma_{-5}^B$	$(\mathbf{1936})\sigma_{\mathbf{-1}}^{\mathbf{B}}$	$(1152)\pi_{-3}$	-
$\lvert 3,-1,-\tilde{1}\rangle_L$	$(16)\sigma_{-5}^v$	$(\mathbf{1936})\sigma_{\mathbf{-1}}^{\mathbf{v}}$	-	$(1152)\pi_{-3}$

Table 2: Transitions between n=3 and n=2 states for the combined Stark-Zeeman effect with the $|n,k,\tilde{m}\rangle_L$ states in the limit $\gamma/\epsilon \to 0$. The notation is similar to that in Table 1. Bold font is used to indicate the strong transitions were σ^v and σ^B derive from different upper-states resulting in a population dependent polarisation orientation.

net polarisation orientation is given by:

$$\theta_\sigma = \arctan\left(\frac{y}{\sqrt{x^2+y^2}+x}\right) \tag{21}$$

$$\begin{aligned} \text{where} \quad y &= 2\delta\cos\psi\sin 2\phi, \\ x &= \sin^2\psi - \delta\cos 2\phi(1+\cos^2\psi) \\ \text{and} \quad \delta &= \frac{N_B A_B - N_v A_v}{N_B A_B + N_v A_v}. \end{aligned} \tag{22}$$

Ideally we expect $\theta_\sigma = 0$ from the defined polarimeter axes in Fig. 1. However $\theta_\sigma \neq 0$ when $\delta \neq 0$, $\psi \neq \pi/2$ and $\phi \neq n\pi/2$ implying the σ linear polarisation is not oriented perpendicular to the electric field. Importantly the upper-state population dependent term is restricted to the range $-1 \leq \delta \leq 1$, allowing bounds to be placed on the deviation using geometric factors alone. As an example we consider a DIII-D MSE channel viewing at $R = 1.78$m from the 315° port[15]. The precise values of ψ and ϕ depend on the equilibrium field but this channel is near the magnetic axis so for simplicity the field is taken to be purely in the negative toroidal direction. In this case $\psi = 93.0°$ as the port is slightly below the midplane and $\phi = -174.2°$. If the $N_v \gg N_B$ then $\delta = -1$ such that $\theta_\sigma = 0.31°$. On the other hand if $N_B \gg N_v$ then $\delta = +1$ and $\theta_\sigma = -27.5°$. It should be noted that from this viewing angle the $\bar{s}_0$ intensity is 75 times greater for the σ_v emission than the σ_B emission,

hence the equation becomes highly non-linear as $\delta \to +1$. A more realistic value of δ is considered in the following section.

As highlighted in Table 2, the σ_1^B and σ_1^v emissions arise from different upper-levels, namely $\left|3,1,\tilde{1}\right\rangle_L$ and $\left|3,1,-\tilde{1}\right\rangle_L$ respectively. Hence when $N_{\left|3,1,\tilde{1}\right\rangle_L} \neq N_{\left|3,1,-\tilde{1}\right\rangle_L}$ the σ_1 polarisation orientation will not be orthogonal to **E** and Eq. 21 is required to determine the net orientation. Similarly the σ_{-1} polarisation orientation will depend on the relative population of $N_{\left|3,-1,\tilde{1}\right\rangle_L}$ and $N_{\left|3,-1,-\tilde{1}\right\rangle_L}$. The effect also exists for the weaker $\sigma_{\pm 5}$ lines.

There are 6 different σ_0 transitions in which case δ in Eq. 22 must be determined by summing the $N_i A_i$ terms over each transition. However from Table 2 we see that the transitions only derive from three different upper-states and the σ_0^B and σ_0^v transition rates within the individual states are equal. Essentially $\sum N_B A_B = \sum N_v A_v$ such that $\delta = 0$, implying σ_0 remains polarised perpendicular to **E** independent of the upper-state populations. At this point it is worthwhile clarifying the finding by Yuh (Ref. [8]) that the σ_0^v and σ_0^B emissions have unequal transition rates from the same upper-states. The quantum states[9] used by Yuh are similar to the $|n,k,\tilde{m}\rangle_L$ states here but with a different orthogonalisation of the three degenerate $|3,0,\tilde{m}\rangle_L$ states. The transitions from that particular orthogonalisation are presented in the Appendix in Tbl. B.5 which can be contrasted with Tbl. 2 here. It will be made clear in the following sections why the orthogonalisations here are physically relevant. The more arbitrary states[9] are only acceptable in the case of equally populated upper-states or with an isotropic excitation mechanism.

A second important result follows from Eqs. 18 and 19 relating to the different angular intensity distributions of the σ^B and σ^v emissions. The intensity of a combined σ^B and σ^v line is

$$I_\sigma \propto 1 + \cos^2\psi - \delta \cos 2\phi \sin^2\psi. \tag{23}$$

Thus a σ line may have an upper-state population dependent intensity when viewing with $\psi \neq 0, \pi$ and $\phi \neq (2n+1)\pi/4$. Eq. 23 is primarily relevant to both the $\sigma_{\pm 1}$ emissions as their σ^B and σ^v transitions derive from different upper-states. This possible effect is overlooked for the B-Stark diagnostic in Ref. [4] that presumes the $\sigma_{\pm 1} : \pi_{\pm 3}$ intensity ratio is independent of the relative upper-state populations.

4.1. Relative upper-state populations

The significance of Eqs. 21 and 23 hinges on the relative populations of pairs of upper-states, expressed in the δ term. For this reason the possibility for unequally populated upper-state pairs is now considered. In the limit that $\gamma = 0$ the probability densities for the Stark-Zeeman states can be expressed in spherical coordinates (r, ψ, ϕ) as,

$$\left| \left| n, k, m \right\rangle_C \right|^2 = f_{nk|m|}(r, \psi), \tag{24}$$

$$\left| \left| n, k, \tilde{m} \right\rangle_L \right|^2 = \begin{cases} 2\cos^2(\tilde{m}\phi) f_{nk|\tilde{m}|}(r, \psi) & \tilde{m} > 0 \\ 2\sin^2(\tilde{m}\phi) f_{nk|\tilde{m}|}(r, \psi) & \tilde{m} < 0. \end{cases} \tag{25}$$

The probability densities for the 'circular' states are independent of ϕ and symmetric about the electric field axis as expected. Whereas the probability densities for the degenerate 'linear' states have a dependence on ϕ that is significantly different for the relevant pairs of degenerate states. Anisotropic excitation mechanisms may therefore have the potential to preferentially excite one degenerate state over the other, an effect that is not considered in Ref. [13] where parabolic state populations are used for $|n, k, \tilde{m}\rangle_L$ like states.

In our coordinate system the neutral beam atom velocity lies in the xy-plane when the electric field is purely motional. The strongest excitation mechanism for the neutral beam atoms is anisotropic collisions with fully stripped plasma ions, with most excitations coming from the ground state. The proton impact excitation cross sections for the perturbed states can be expressed in terms of excitation cross sections σ_{nl_m} for the $|n, l, m\rangle$ states with quantisation axis in the direction of the neutral beam atoms[16]. Cross sections for proton impact excitation from the ground state to the parabolic n=2 and n=3 levels are given in Refs. [17] and [16] respectively. As expected from the symmetry in Eq. 24, degenerate pairs of upper-states individually producing σ^+ and σ^- for a given energy in Table 1 are predicted to have the same cross sections and populations.

The ground state proton impact excitation cross sections for the degenerate $|n, k, \tilde{m}\rangle_L$ pairs however are dependent on the beam injection angle ρ

relative to the magnetic field and are given by ($\gamma \ll \epsilon$):

$$\sigma_{|2,0,\tilde{1}\rangle_L} = \cos^2\rho\ \sigma_{2p_0} + \sin^2\rho\ \sigma_{2p_1}, \tag{26}$$

$$\sigma_{|2,0,-\tilde{1}\rangle_L} = \sin^2\rho\ \sigma_{2p_0} + \cos^2\rho\ \sigma_{2p_1}, \tag{27}$$

$$\sigma_{|3,0,\tilde{2}\rangle_L} = \frac{1}{4}\cos^2 2\rho\,(3\sigma_{3d_0} + \sigma_{3d_2}) + \sin^2 2\rho\ \sigma_{3d_1}, \tag{28}$$

$$\sigma_{|3,0,-\tilde{2}\rangle_L} = \frac{1}{4}\sin^2 2\rho\,(3\sigma_{3d_0} + \sigma_{3d_2}) + \cos^2 2\rho\ \sigma_{3d_1}, \tag{29}$$

$$\sigma_{|3,\pm1,\tilde{1}\rangle_L} = \frac{1}{2}\cos^2\rho\,(\sigma_{3p_0} + \sigma_{3d_1}) + \frac{1}{2}\sin^2\rho\ \ (\sigma_{3p_1} + \sigma_{3d_2}), \tag{30}$$

$$\sigma_{|3,\pm1,-\tilde{1}\rangle_L} = \frac{1}{2}\sin^2\rho\,(\sigma_{3p_0} + \sigma_{3d_1}) + \frac{1}{2}\cos^2\rho\ (\sigma_{3p_1} + \sigma_{3d_2})\,. \tag{31}$$

For a radially injected beam, that is $\rho = 90°$, the $|3,1,\pm\tilde{1}\rangle_L$ cross section are the maximally different, suggesting unequal populations and a σ_1 linear polarisation non-orthogonal to **E**, particularly when gas or plasma densities are low. However if $\rho = 45°$ the cross sections for the $|3,1,\pm\tilde{1}\rangle_L$ pair are equal, suggesting equal populations and in turn σ_1 polarised orthogonal to **E** as desired. A similar argument is true for the $|3,-1,\pm\tilde{1}\rangle_L$ pair and the σ_{-1} emission.

For the DIII-D example in the previous section the beam is injected at angle $\rho = 49.6°$ with an energy of 40keV/u. The cross sections needed in Eqs. 30 and 31 are found in Ref. [16] to be $\sigma_{3p_0} = 0.058\pi a_0^2$, $\sigma_{3p_1} = 0.038\pi a_0^2$, $\sigma_{3d_1} = 0.010\pi a_0^2$ and $\sigma_{3d_2} = 0.002\pi a_0^2$ such that $\sigma_{|3,\pm1,\tilde{1}\rangle_L} = 0.026\pi a_0^2$ and $\sigma_{|3,\pm1,-\tilde{1}\rangle_L} = 0.028\pi a_0^2$. Naively assuming this is the only excitation pathway provides an estimate for the population factor of $\delta = -0.041$ in the low density limit. The actual value of δ is expected to be closer to zero when further excitation pathways are considered and as statistical populations are approached, more so for beam into plasma shots. From Eq. 21 this corresponds to a deviation of $\theta_{\sigma_{\pm1}} = 0.024°$ which is smaller than the $\sim 0.1°$ measurement accuracy often targeted for polarimetric MSE measurements.

5. Degeneracy splitting of the fine-structure

To this point the observable differences between the $|n,k,m\rangle_C$, $|n,k,\tilde{m}\rangle_L$ and Ref. [9] Stark-Zeeman states have been described, but it is not yet possible to know which is actually physical as the system is underdetermined. Weaker interactions that completely resolve the remaining degeneracy and

determine the system must first be considered. For this reason the outcomes of a model are more sensitive to the implementation of weaker interactions than expected.

The fine-structure of the atom is the largest fixed interaction after the linear Stark and Zeeman effects. It breaks the remaining degeneracy in the Stark-Zeeman levels which in turn determines the states and polarisation structure. The fine-structure leads to unwieldy solutions but similarities exist with the analytic Stark-Zeeman solutions presented here. For the magnetic field strengths and neutral beam velocities encountered in fusion devices the fine-structure breaks the remaining degeneracy such the Stark-Zeeman-fine-structure states are similar to the $|n, k, \tilde{m}\rangle_L$ states and reduce to them when the Stark and Zeeman effect dominate the fine-structure.

Previously the electron spin has been unimportant (Paschen-Back regime) as it only offsets the energy levels but transitions between opposite spin states are forbidden. Including the fine-structure requires account of electron spin, however the splitting and shifts it introduces are relatively small and transitions between states of opposite spin remain weak. Thus Table 2 still provides a good approximation of the Stark-Zeeman-fine-structure transitions and the phenomena discussed in the previous section are therefore relevant.

Now that the fine-structure has also been considered conclusion can be drawn about the existing models that also include interactions beyond the Stark and Zeeman effects. In particular it has been shown for the $|n, k, \tilde{m}\rangle_L$ states that the linear polarisation orientation of the σ_0 emission remains orthogonal to $\mathbf{E}$ when upper-state populations are non-statistical. This contradicts the data presented in Figure 13 of Ref. [6] that indicates that the σ_0 polarisation can deviate by several degrees between beam into gas and plasma shots. We have tested a recent 'bug' fix made in 2015 to the implementation of the Zeeman effect in the 'Flexible Atomic Code'[7] and found that it alters the more accessible result in Figure 1 of Ref. [6]. This 'bug' has possibly contributed to the predicted σ_0 deviation that disagrees with the result that is presented here. The diamagnetic Zeeman effect included in Ref. [6] has been tested in calculations here and found to have a negligible effect on the results, in agreement with the assessment in Ref. [14].

The $\sigma_{\pm 1}$ and $\pi_{\pm_3}$ emission derive from the same upper $|n, k, \tilde{m}\rangle_L$ states with comparable transition probability ratios. This is in agreement with pure Stark theory[3] but contradicts Table 1 in Ref. [5] that suggests there are n=3 levels emitting only $\pi_{\pm 3}$ without any $\sigma_{\pm 1}$. The cause of this disagreement is unknown but the calculation method used here is thought to be effectively

the same.

6. Degeneracy splitting of microscopic electric fields

In Sec. 3 the electric and magnetic fields were allowed to be non-orthogonal ($\tau \neq 0$) to generate the $|n,k,m\rangle_C$ states in the limit $\tau \to 0$. Fluctuating microscopic electric fields within the plasma may have a component parallel to the magnetic field and will superpose with the motional electric field such that $\tau \neq 0$. Evidently there must be a crossover point where the microscopic electric field is sufficiently large to break the degeneracy in favour of the $|n,k,m\rangle_C$ states and overcomes the degeneracy splitting of the fine-structure which favoured the $|n,k,\tilde{m}\rangle_L$ states.

The Holtsmark field strength $|\mathbf{E_0}| = 2.6en_e^{2/3}/(4\pi\epsilon_0)$ provides a characteristic strength for the distribution of microscopic fields in a plasma of electron density n_e[18]. Requiring the microscopic field component to be parallel to the magnetic field results in an average reduction of 1/2. Thus for a $n_e = 10^{20}\mathrm{m}^{-3}$ plasma we have $|\mathbf{E_0}|/2 = 40\mathrm{kV\,m}^{-1}$ which compares with an example motional electric field of $4.8\mathrm{MV\,m}^{-1}$ produced by injecting an 80keV deuterium beam at 60° to a 2T field.

The $|3,\pm1,\pm\tilde{1}\rangle_L$ Stark-Zeeman states are of the most concern for the linear polarisation orientation as they individually produce $\sigma^B_{\pm1}$ or $\sigma^v_{\pm1}$ emissions. The fine-structure splits the Stark-Zeeman degenerate $|3,1,\pm\tilde{1},+\rangle$ levels by 0.5μeV, where the + sign is used to indicate the sign of the energy shift resulting from the electron spin. A parallel microscopic electric field becomes the dominant degeneracy splitting mechanism for strengths above $10\mathrm{kV\,m}^{-1}$ as seen in Fig. 4a). The similarity of the states to the $|n,k,\tilde{m}\rangle_L$ and $|n,k,m\rangle_C$ bases is best visualised from $\langle L_z\rangle$ plotted in Fig. 4b). Over the range of $1 - 50\mathrm{kV\,m}^{-1}$ the states transform from being similar to the $|3,1,\pm\tilde{1}\rangle_L$ states to being similar to the $|3,1,\pm1\rangle_C$ states. Therefore with increasing microscopic field the polarisation structure transforms from the upper-state population dependent σ^B_1 and σ^v_1 emission to the 'robust' σ^+_1 and σ^-_1 emission. For intermediate values of $\langle L_z\rangle$ the $\sigma_{\pm1}$ transitions will be elliptical with major-axes aligned along $\mathbf{B}$ and $\mathbf{v}\times\mathbf{B}$.

Each beam atom in the plasma will be subjected to a different microscopic electric fields from the distribution so in reality there will be a mixture of $|n,k,\tilde{m}\rangle_L$, $|n,k,m\rangle_C$ and intermediate states. Overall this will result in a more robust $\sigma_{\pm1}$ polarisation orientation than from the $|n,k,\tilde{m}\rangle_L$ states alone.

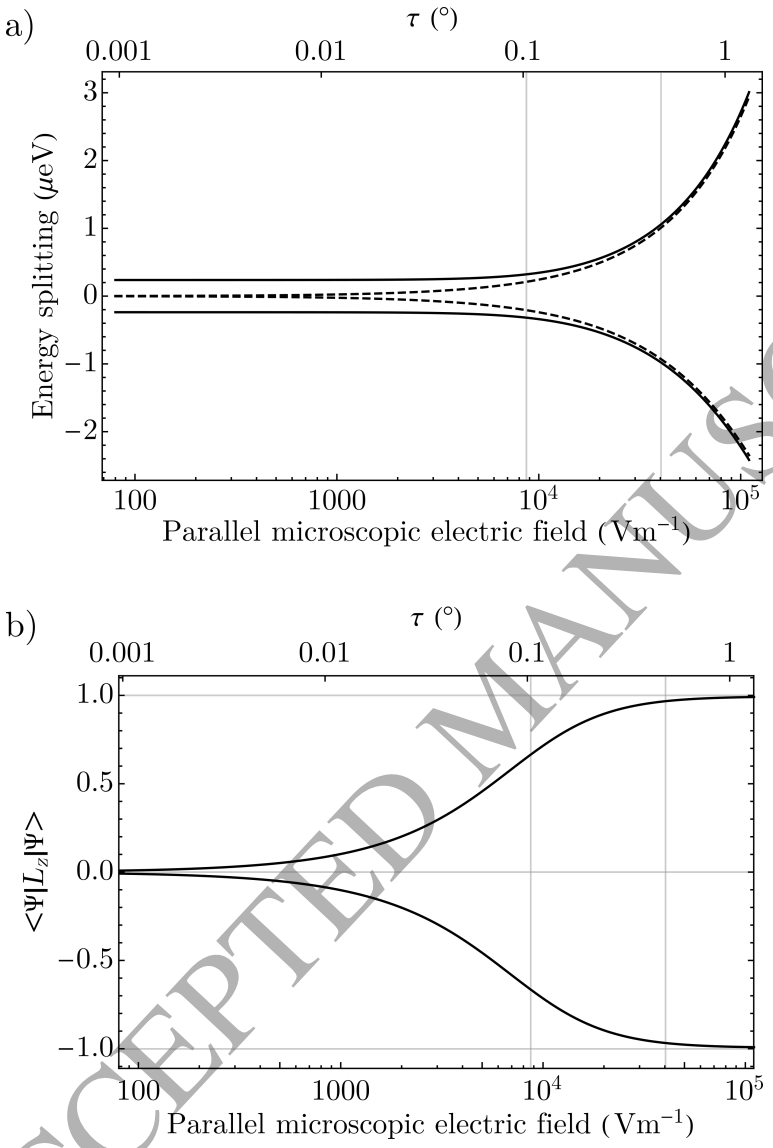

Figure 4: a) Degeneracy splitting when including an electric field component parallel to the magnetic field ($\tau \neq 0$). The dashed lines are the energy of the Stark-Zeeman $|3,1,\pm1\rangle$ levels given in Eq. 10. The solid lines are the energy splitting of the Stark-Zeeman-fine-structure $|3,1,\pm\tilde{1},+\rangle$ states. Offsets between the two cases have been removed. The left and right vertical gridlines indicate 50% of the Holtsmark field strength for plasma densities of $10^{19}\mathrm{m}^{-3}$ and $10^{20}\mathrm{m}^{-3}$ respectively (see text). b) Expectation value of angular momentum in the direction of the total electric field for the $|3,1,\pm\tilde{1},+\rangle$ states.

The $\left|3,0,\pm\tilde{2}\right\rangle$ Stark-Zeeman-fine-structure states have almost identical energies with less than 1neV separation. Therefore a weaker parallel electric field is required to overcome the effects of the fine-structure. These states transform from being like the $\left|3,0,\pm\tilde{2}\right\rangle_L$ states to the $|3,0,\pm2\rangle_C$ states over the range $0.01-5\mathrm{V\,m^{-1}}$. Meanwhile the fine-structure splits the $\left|2,0,\pm\tilde{1}\right\rangle$ levels by about 0.4μeV requiring a parallel microscopic electric field of $1-50\mathrm{kV\,m^{-1}}$ to transform to the $|2,0,\pm1\rangle_C$ similar states.

Although microscopic electric fields will change the orientation of each emission slightly, the net effect is expected to average to the macroscopic field. Radial electric fields in the plasma are orthogonal to $\mathbf{B}$ and therefore may change the polarisation orientation without affecting the underlying polarisation structure.

7. Conclusion

Degeneracy in the Stark-Zeeman energy levels when $\mathbf{E}\perp\mathbf{B}$ leads to an underdetermined polarisation structure for the Balmer-alpha emission. The polarisation structure is therefore sensitive to the weaker interactions that resolve this degeneracy and neglecting these weaker interactions can have significant effects on the predictions of a model.

The linear polarisation orientation of the σ_0 and π emissions are predicted to be an accurate measure of the electric field orientation in both plasma shots and BIG, independent of the density and upper-state populations. However, there is a possibility for the $\sigma_{\pm1}$ linear polarisation to deviate from prediction based on the pure Stark effect, summarised in Eq. 21. The deviation for plasma shots is expected to be $\ll 0.1°$ owing to: higher densities producing more statistical upper-state populations, high electron densities contributing a microscopic electric field that breaks the degeneracy in favour of the more 'robust' $|n,k,m\rangle_C$ states, beam injection angles close to $\rho=45°$ creating more equally populated upper-state pairs, the greater intensity and throughput of σ_0 relative to $\sigma_{\pm1}$, and using viewing directions with a significant component perpendicular to the motional electric field and parallel/antiparallel to the magnetic field.

For BIG the lower densities suggest greater differences in the upper-state populations and the lack of free charges contributing microscopic electric fields indicate the beam atoms will adopt the $\left|n,k,\tilde{m}\right\rangle_L$ like states. Nevertheless with standard tangential viewing geometries and beam injection

angles near 45° the $\sigma_{\pm1}$ polarisation orientation deviation can also be negligible. There is no reported evidence that the measured σ linear polarisation orientation deviates with a viewing angle dependence given in Eq. 21 or that the deviation increases at lower gas densities. Discrepancies in BIG data are often attributed to emission from secondary neutrals which predicts greater errors at higher gas densities. Therefore the polarisation structure effects presented here and secondary neutral effects should be distinguishable. Polarisation sensitive spectrometer measurements that resolve the central σ peak into its three components are needed to unambiguously resolve this effect. Such a measurement would require a device with large Stark splitting, a beam injection angle away from $\rho = 45°$ and a viewing geometry away from $\psi = \pi/2$ and $\phi = 0$ which are not typically employed.

BIG calibration of the $\sigma_{\pm1} : \pi_{\pm3}$ intensity ratio is susceptible to upper-state population effects for similar reasons that apply to the $\sigma_{\pm1}$ polarisation measurements.

Acknowledgments

The author acknowledges useful discussions with J. Howard and C. Michael, and would like to thank AINSE Ltd for providing financial assistance (Award - PGRA) to enable this work.

References

[1] F. M. Levinton, R. J. Fonck, G. M. Gammel, R. Kaita, H. W. Kugel, E. T. Powell, D. W. Roberts, Magnetic field pitch-angle measurments in the PBX-M tokamak using the motional Stark effect, Phys. Rev. Lett. 63 (19) (1989) 2060–2063. doi:10.1103/PhysRevLett.63.2060.
URL http://link.aps.org/doi/10.1103/PhysRevLett.63.2060

[2] A. Boileau, M. von Hellerman, W. Mandl, H. P. Summers, H. Weisen, A. Zinoviev, Observations of motional Stark features in the Balmer spectrum of deuterium in the JET plasma, Journal of Physics B: Atomic, Molecular and Optical Physics 22 (7) (1989) L145. doi:10.1088/0953-4075/22/7/002.
URL http://stacks.iop.org/0953-4075/22/i=7/a=002

[3] H. A. Bethe, E. E. Salpeter, Quantum Mechanics of One- and Two-Electron Atoms, Springer US, Boston, MA, 1977. doi:10.1007/

978-1-4613-4104-8.
URL http://link.springer.com/10.1007/978-1-4613-4104-8

[4] N. A. Pablant, K. H. Burrell, R. J. Groebner, C. T. Holcomb, D. H. Kaplan, Measurements of the internal magnetic field using the B-Stark motional Stark effect diagnostic on DIII-D (invited)a), Review of Scientific Instruments 81 (10) (2010) 10D729. doi:http://dx.doi.org/10.1063/1.3491209.
URL http://scitation.aip.org/content/aip/journal/rsi/81/10/10.1063/1.3491209

[5] A. Iwamae, A. Sakaue, M. Atake, K. Sawada, M. Goto, S. Morita, Alignment creation and deviation from statistical population distribution in hydrogen n = 3 levels observed on MSE spectra of LHD plasma, Plasma Physics and Controlled Fusion 51 (11) (2009) 115004. doi:10.1088/0741-3335/51/11/115004.
URL http://stacks.iop.org/0741-3335/51/i=11/a=115004?key=crossref.ee8945769f7215e50fbb6c19deb3d327http://stacks.iop.org/0741-3335/51/i=11/a=115004

[6] M. F. Gu, C. T. Holcomb, R. J. Jayakuma, S. L. Allen, Atomic models for the motional Stark effect diagnostic, Journal of Physics B: Atomic, Molecular and Optical Physics 41 (9) (2008) 95701. doi:10.1088/0953-4075/41/9/095701.
URL http://iopscience.iop.org/0953-4075/41/9/095701{%}5Cnhttp://iopscience.iop.org/0953-4075/41/9/095701/{%}5Cnhttp://iopscience.iop.org/0953-4075/41/9/095701/pdf/0953-4075{_}41{_}9{_}095701.pdfhttp://stacks.iop.org/0953-4075/41/i=9/a=095701

[7] E. Stambulchik, FAC Changelog (2017).
URL https://github.com/fnevgeny/fac/blob/master/ChangeLog

[8] H. Y. H. Yuh, The Motional Stark Effect Diagnostic on Alcator C-Mod, Ph.D. thesis, Massachusetts Institute of Technology (2005).
URL http://hdl.handle.net/1721.1/34976

[9] R. C. Isler, Profiles and polarizations of the Balmer- α line from high-temperature hydrogen atoms in strong magnetic fields, Physical Review

A 14 (3) (1976) 1015–1019. doi:10.1103/PhysRevA.14.1015.
URL http://link.aps.org/doi/10.1103/PhysRevA.14.1015

[10] O. Marchuk, Y. Ralchenko, R. K. Janev, W. Biel, E. Delabie, a. M. Urnov, Collisional excitation and emission of H α Stark multiplet in fusion plasmas, Journal of Physics B: Atomic, Molecular and Optical Physics 43 (1) (2010) 11002. doi:10.1088/0953-4075/43/1/011002.
URL http://stacks.iop.org/0953-4075/43/i=1/a=011002?key=crossref.ad6c5fab6ab553ee76cae4bb0e256cddhttp://stacks.iop.org/0953-4075/43/i=1/a=011002

[11] H. Y. Yuh, F. M. Levinton, S. D. Scott, J. Ko, Simulation of the motional Stark effect diagnostic gas-filled torus calibrationa), Review of Scientific Instruments 79 (10) (2008) 10F523. doi:http://dx.doi.org/10.1063/1.2969419.
URL http://scitation.aip.org/content/aip/journal/rsi/79/10/10.1063/1.2969419

[12] B. S. Victor, C. T. Holcomb, S. L. Allen, W. H. Meyer, M. A. Makowski, A. Thorman, Asymmetries in the motional Stark effect emission on the DIII-D tokamak, Review of Scientific Instruments 87 (11) (2016) 11E126. doi:10.1063/1.4961560.
URL http://scitation.aip.org/content/aip/journal/rsi/87/11/10.1063/1.4961560

[13] R. Reimer, O. Marchuk, B. Geiger, P. J. Mc Carthy, M. Dunne, J. Hobirk, R. Wolf, A. U. Team, Influence of non-local thermodynamic equilibrium and Zeeman effects on magnetic equilibrium reconstruction using spectral motional Stark effect diagnostic, Review of Scientific Instruments 88 (8) (2017) 083509. doi:10.1063/1.4994889.
URL http://dx.doi.org/10.1063/1.4994889http://aip.scitation.org/toc/rsi/88/8

[14] E. K. Souw, J. Uhlenbusch, Calculation of the combined Zeeman and translational Stark effect on the Hα-multiplet, Physica B+C 122 (3) (1983) 353–374. doi:http://dx.doi.org/10.1016/0378-4363(83)90063-3.
URL http://www.sciencedirect.com/science/article/pii/0378436383900633

[15] C. T. Holcomb, M. A. Makowski, R. J. Jayakumar, S. A. Allen, R. M. Ellis, R. Geer, D. Behne, K. L. Morris, L. G. Seppala, J. M. Moller, Motional Stark effect diagnostic expansion on DIII-D for enhanced current and Er profile measurements, Review of Scientific Instruments 77 (10) (2006) 10E506. doi:10.1063/1.2235812.
URL http://aip.scitation.org/doi/10.1063/1.2235812

[16] O. Marchuk, Y. Ralchenko, D. R. Schultz, Non-statistical population distributions for hydrogen beams in fusion plasmas, Plasma Physics and Controlled Fusion 54 (9) (2012) 95010. doi:10.1088/0741-3335/54/9/095010.
URL http://stacks.iop.org/0741-3335/54/i=9/a=095010http://stacks.iop.org/0741-3335/54/i=9/a=095010?key=crossref.6360a897408fde4446a89625fd89c1ca

[17] O. Marchuk, Y. Ralchenko, D. R. Schultz, E. Delabie, A. M. Urnov, W. Biel, R. K. Janev, T. Schlummer, Non-statistical simulations for neutral beam spectroscopy in fusion plasmas, AIP Conference Proceedings 1438 (1) (2012) 169–174. doi:http://dx.doi.org/10.1063/1.4707873.
URL http://scitation.aip.org/content/aip/proceeding/aipcp/10.1063/1.4707873

[18] H. R. Griem, Spectral Line Broadening by Plasmas, Vol. Volume 39, Academic Press, 1974.

[19] A. E. Kramida, A critical compilation of experimental data on spectral lines and energy levels of hydrogen, deuterium, and tritium, Atomic Data and Nuclear Data Tables 96 (6) (2010) 586–644. doi:http://dx.doi.org/10.1016/j.adt.2010.05.001.
URL http://www.sciencedirect.com/science/article/pii/S0092640X10000458

Appendix A. Perturbation Theory

The deuterium wave functions in the presence of electric and magnetic fields are calculated using first order perturbation theory. While an emphasis is placed on MSE measurements, the calculations are general and treat ϵ and

γ independently. The Hamiltonian for the system is

$$H = H_0 + H_E + H_B, \tag{A.1}$$
$$H_E = e|\mathbf{E}|z, \tag{A.2}$$
$$H_B = \frac{e|\mathbf{B}|}{2m_e}\Big((g_l L_x + g_s S_x)\cos\tau + (g_l L_z + g_s S_z)\sin\tau\Big), \tag{A.3}$$

where H_0 is the unperturbed Hamiltonian including fine-structure, $g_l = 1$ is the orbital g-factor, $g_s = 2.0023$ is the spin-g-factor and s is the spin operator. The calculations are performed in the well known hydrogen/deuterium wavefunction $|n, l, m_l, m_s\rangle$ basis. A shorthand notation $|\Phi_{n,\alpha}\rangle$ is used for this basis, where Greek subscript are used to represent the allowable combinations of the l, m_l and m_s quantum numbers. The first step is to calculate the Hamiltonian matrix elements $H_{n,\alpha\beta} = \langle\Phi_{n,\alpha}|H|\Phi_{n,\beta}\rangle$. The Stark and Zeeman Hamiltonian components are straightforward to integrate with Wolfram Mathematica. H_0 is diagonal in the $|n, l, j, m_j\rangle$ basis with values tabulated to high precision[19] and can be converted to the $|n, l, m, m_s\rangle$ basis with Clebsch-Gordon coefficients.

The i^{th} eigenvector, $b_{n,i\eta}$, of the $H_{n,\alpha\beta}$ matrix determines the mixing coefficients such that the perturbed wave functions are $|\Psi_{n,i}\rangle = \sum_\eta b_{n,i\eta}\,|\Phi_{n,\eta}\rangle$ and the energy of state $|\Psi_{n,i}\rangle$ is the corresponding eigenvalue $E_{n,i}$. The dipole vector describing the polarisation of a transition between the n=3 and n=2 levels is

$$\begin{aligned}\mathbf{r}_{ij} &= \langle\Psi_{2,i}\,|\,\mathbf{r}\,|\,\Psi_{3,j}\rangle \\ &= \sum_{\alpha\beta} b^*_{2,i\alpha} b_{3,j\beta}\,\langle\Phi_{2,\alpha}\,|\,\mathbf{r}\,|\,\Phi_{3,\beta}\rangle\,.\end{aligned} \tag{A.4}$$

Integration of the $\langle\Phi_{2,\alpha}\,|\,\mathbf{r}\,|\,\Phi_{3,\beta}\rangle$ terms is straightforward with Mathematica. In general the real part of $(\mathbf{r}_{ij}e^{-\iota\omega_{ij}t})$ traces out an ellipse in time with angular frequency $\omega_{ij} = (E_{3,j} - E_{2,i})/\hbar$. The spontaneous emission rate coefficient for a particular transition is

$$A_{ij} = \frac{e^2\omega^3_{ij}}{3\pi\epsilon_0\hbar c^3}\,|\mathbf{r}_{ij}|^2\,. \tag{A.5}$$

The observed polarisation of the emission is dependent on the viewing direction and is obtained by taking the projection of the dipole vector. The

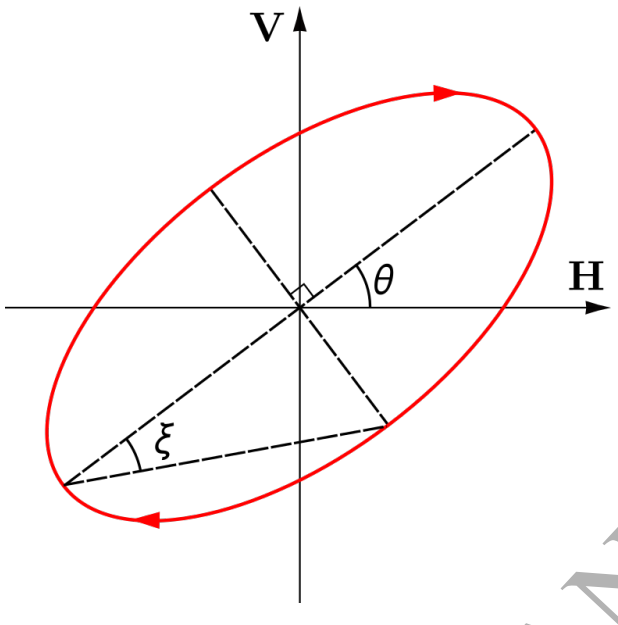

Figure A.5: Polarisation ellipse observed from point of view of the detector. The elliptical polarisation is right handed such that $\xi > 0$ ($s_3 > 0$).

polarimeter axes are defined in Fig. A.5 such that the projected dipole vector and dimensionless Stokes vector for each transition are:

$$(r_H)_{ij} = \mathbf{r}_{ij}.\hat{\mathbf{H}}, \tag{A.6}$$

$$(r_V)_{ij} = \mathbf{r}_{ij}.\hat{\mathbf{V}}, \tag{A.7}$$

$$\begin{aligned}\bar{\mathbf{s}} &= (\bar{s}_0,\, \bar{s}_1,\, \bar{s}_2,\, \bar{s}_3) \\ &= \frac{1}{|\mathbf{r}|^2}\big(|r_H|^2 + |r_V|^2,\, |r_H|^2 - |r_V|^2, \\ &\quad 2\,\mathrm{Re}[r_H r_V^*],\, 2\,\mathrm{Im}[r_H r_V^*]\big),\end{aligned} \tag{A.8}$$

where the ij subscript is implied for each term in Eq. A.8. The Stokes vector describes the polarisation ellipse traced out by the light wave's electric field in time at the detector which can be expressed in geometric terms as

$$\bar{\mathbf{s}} = \bar{s}_0(1,\, p\cos 2\xi \cos 2\theta,\, p\cos 2\xi \sin 2\theta,\, p \sin 2\xi), \tag{A.9}$$

where p is the degree of polarisation, θ is the orientation of the polarisation ellipse's major-axis and ξ is it's ellipticity angle, as defined in Fig. A.5.

The Stokes vector (power per unit solid angle) for the emission is then

$$\mathbf{s}(\omega) = \frac{3}{8\pi} \sum_j N_{3,j} \sum_i \hbar\omega_{ij} A_{ij} \bar{\mathbf{s}}_{ij}(\omega), \tag{A.10}$$

where $N_{3,j}$ is the population of beam atoms within the viewing volume in the $|\Psi_{3,j}\rangle$ state. We ignore the apparent spectral broadening effects due to the line of sight integration. In Eq. A.10 there are $8 \times 18 = 144$ summed transitions (when electron spin is included) for which the Stokes vectors are summed incoherently.

Appendix B. Stark-Zeeman Tables

State	$\|2,1,0\rangle_C$	$\|2,-1,0\rangle_C$	$\|2,0,1\rangle_C$	$\|2,0,-1\rangle_C$
$\|2,0,0\rangle$	$\sqrt{2}\epsilon$	$\sqrt{2}\epsilon$	$\sqrt{2}\gamma$	$\sqrt{2}\gamma$
$\|2,1,0\rangle$	$-\sqrt{2}q_0$	$\sqrt{2}q_0$	0	0
$\|2,1,1\rangle$	$-\gamma$	$-\gamma$	$\epsilon + q_0$	$\epsilon - q_0$
$\|2,1,-1\rangle$	$-\gamma$	$-\gamma$	$\epsilon - q_0$	$\epsilon + q_0$

Table B.3: Mixing coefficients $b_{2,kl}$ for the 'circular' Stark-Zeeman n=2 states such that $|2,k,m\rangle_C = \sum b_{2,kl}\,|2,l,m\rangle$. The coefficients must be normalised by $2q_0$. The $|n,k,m\rangle_C$ states reduce to the parabolic states when $\gamma = 0$.

State	$\|3,2,0\rangle_C$	$\|3,-2,0\rangle_C$	$\|3,0,0\rangle_C$	$\|3,0,2\rangle_C$	$\|3,0,-2\rangle_C$	$\|3,1,1\rangle_C$	$\|3,1,-1\rangle_C$	$\|3,-1,1\rangle_C$	$\|3,-1,-1\rangle_C$
$\|3,0,0\rangle$	$18\sqrt{2}\epsilon^2$	$18\sqrt{2}\epsilon^2$	$2\sqrt{2}(9\epsilon^2 - 4\gamma^2)$	$8\sqrt{2}\gamma^2$	$8\sqrt{2}\gamma^2$	$24\gamma\epsilon$	$24\gamma\epsilon$	$24\gamma\epsilon$	$24\gamma\epsilon$
$\|3,1,0\rangle$	$-6\sqrt{3}\epsilon q_1$	$6\sqrt{3}\epsilon q_1$	0	0	0	$-2\sqrt{6}\gamma q_1$	$-2\sqrt{6}\gamma q_1$	$2\sqrt{6}\gamma q_1$	$2\sqrt{6}\gamma q_1$
$\|3,2,0\rangle$	$6(3\epsilon^2 + 2\gamma^2)$	$6(3\epsilon^2 + 2\gamma^2)$	$-4(9\epsilon^2 + 2\gamma^2)$	$-4\gamma^2$	$-4\gamma^2$	$-6\sqrt{2}\gamma\epsilon$	$-6\sqrt{2}\gamma\epsilon$	$-6\sqrt{2}\gamma\epsilon$	$-6\sqrt{2}\gamma\epsilon$
$\|3,2,2\rangle$	$2\sqrt{6}\gamma^2$	$2\sqrt{6}\gamma^2$	$4\sqrt{6}\gamma^2$	$\sqrt{6}(9\epsilon^2 + 3\epsilon q_1 + 2\gamma^2)$	$\sqrt{6}(9\epsilon^2 - 3\epsilon q_1 + 2\gamma^2)$	$-2\sqrt{3}\gamma(q_1 + 3\epsilon)$	$2\sqrt{3}\gamma(q_1 - 3\epsilon)$	$-2\sqrt{3}\gamma(q_1 + 3\epsilon)$	$2\sqrt{3}\gamma(q_1 - 3\epsilon)$
$\|3,2,-2\rangle$	$2\sqrt{6}\gamma^2$	$2\sqrt{6}\gamma^2$	$4\sqrt{6}\gamma^2$	$\sqrt{6}(9\epsilon^2 - 3\epsilon q_1 + 2\gamma^2)$	$\sqrt{6}(9\epsilon^2 + 3\epsilon q_1 + 2\gamma^2)$	$2\sqrt{3}\gamma(q_1 - 3\epsilon)$	$-2\sqrt{3}\gamma(q_1 + 3\epsilon)$	$2\sqrt{3}\gamma(q_1 - 3\epsilon)$	$-2\sqrt{3}\gamma(q_1 + 3\epsilon)$
$\|3,1,1\rangle$	$-6\sqrt{6}\gamma\epsilon$	$-6\sqrt{6}\gamma\epsilon$	$-12\sqrt{6}\gamma\epsilon$	$2\sqrt{6}\gamma(3\epsilon + q_1)$	$2\sqrt{6}\gamma(3\epsilon - q_1)$	$\sqrt{3}(9\epsilon^2 + 3\epsilon q_1 - 4\gamma^2)$	$\sqrt{3}(9\epsilon^2 - 3\epsilon q_1 - 4\gamma^2)$	$\sqrt{3}(9\epsilon^2 + 3\epsilon q_1 - 4\gamma^2)$	$\sqrt{3}(9\epsilon^2 - 3\epsilon q_1 - 4\gamma^2)$
$\|3,2,1\rangle$	$2\sqrt{6}\gamma q_1$	$-2\sqrt{6}\gamma q_1$	0	0	0	$-\sqrt{3}q_1(q_1 + 3\epsilon)$	$\sqrt{3}q_1(q_1 - 3\epsilon)$	$\sqrt{3}q_1(q_1 + 3\epsilon)$	$-\sqrt{3}q_1(q_1 - 3\epsilon)$
$\|3,1,-1\rangle$	$-6\sqrt{6}\gamma\epsilon$	$-6\sqrt{6}\gamma\epsilon$	$-12\sqrt{6}\gamma\epsilon$	$2\sqrt{6}\gamma(3\epsilon - q_1)$	$2\sqrt{6}\gamma(3\epsilon + q_1)$	$\sqrt{3}(9\epsilon^2 - 3\epsilon q_1 - 4\gamma^2)$	$\sqrt{3}(9\epsilon^2 + 3\epsilon q_1 - 4\gamma^2)$	$\sqrt{3}(9\epsilon^2 - 3\epsilon q_1 - 4\gamma^2)$	$\sqrt{3}(9\epsilon^2 + 3\epsilon q_1 - 4\gamma^2)$
$\|3,2,-1\rangle$	$2\sqrt{6}\gamma q_1$	$-2\sqrt{6}\gamma q_1$	0	0	0	$\sqrt{3}q_1(q_1 - 3\epsilon)$	$-\sqrt{3}q_1(q_1 + 3\epsilon)$	$-\sqrt{3}q_1(q_1 - 3\epsilon)$	$\sqrt{3}q_1(q_1 + 3\epsilon)$

Table B.4: Mixing coefficients $b_{3,kl}$ for the 'circular' Stark-Zeeman n=3 states such that $|3,k,m\rangle_C = \sum b_{3,kl}\,|3,l,m\rangle$. The coefficients must be normalised by $2\sqrt{6}q_1^2$. The table simplifies to the parabolic states when $\gamma = 0$.

$\|n,k,m_l\rangle$	Tbl.III 2^{nd}	Tbl.III 3^{rd}	Tbl.III 4^{th}	Tbl.III 1^{st}
Tbl.I 1^{st}	$(1681)\pi_4$	$(1)\pi_8$	$(18)\sigma_6^B$	$(18)\sigma_6^v$
Tbl.I 2^{nd}	$(1)\pi_{-8}$	$(1681)\pi_{-4}$	$(18)\sigma_{-6}^B$	$(18)\sigma_{-6}^v$
Tbl.I 5^{th}	$(486)\pi_{-2}$	$(486)\pi_2$	$(\mathbf{12})\sigma_{\mathbf{0}}^{\mathbf{B}}$	$(\mathbf{2700})\sigma_{\mathbf{0}}^{\mathbf{v}}$
Tbl.II 1^{st}	-	-	$(2304)\sigma_0^v$	$(2304)\sigma_0^B$
Tbl.I 6^{th}	$(243)\pi_{-2}$	$(243)\pi_2$	$(\mathbf{3174})\sigma_{\mathbf{0}}^{\mathbf{B}}$	$(\mathbf{486})\sigma_{\mathbf{0}}^{\mathbf{v}}$
Tbl.II 2^{nd}	$(1936)\sigma_1^B$	$(16)\sigma_5^B$	$(1152)\pi_3$	-
Tbl.I 3^{rd}	$(1936)\sigma_1^v$	$(16)\sigma_5^v$	-	$(1152)\pi_3$
Tbl.II 3^{rd}	$(16)\sigma_{-5}^B$	$(1936)\sigma_{-1}^B$	$(1152)\pi_{-3}$	-
Tbl.I 4^{th}	$(16)\sigma_{-5}^v$	$(1936)\sigma_{-1}^v$	-	$(1152)\pi_{-3}$

Table B.5: Transitions between the Stark-Zeeman states of Ref. [9]. The ordering of states is similar to that in Tables 1 and 2